# Manipulation of interfacial ferrimagnetic order via proximity effect in two-dimensional heterostructures $WS_2$/CoTb

Yuzhi Li,[1,2] Jiazhan Chang,[3] Bo Zhang,[1] Lijuan Zhao,[1] Jianrong Zhang,[1] Li Xi,[1] Jiangwei Cao,[1] Yalu Zuo,[1] Junli Zhang,[1] Mingsu Si,[3] Desheng Xue,[1,*] and Dezheng Yang[1,†]

[1]*School of Physical Science and Technology, Lanzhou University, Lanzhou 730000, China*

[2]*School of Physics and Electronic Engineering, Sichuan University of Science and Engineering, Yibin 644000, China*

[3]*School of Materials and Energy, Lanzhou University, Lanzhou 730000, China*

(Received 27 August 2024; revised 27 January 2025; accepted 10 February 2025; published 18 February 2025)

Due to the unique properties of compensated ferrimagnets, such as long spin coherence length, fast domain wall motion, and large spin-orbit torque, to manipulate ferrimagnetic order is crucial in spintronics. Here, we investigate the proximity effect of the two-dimensional van der Waals material $WS_2$ on the interfacial ferrimagnetic order of CoTb. By increasing the thickness of $WS_2$ from one to three layers, a dramatic increase of ferrimagnetic compensation temperature by 75 K is observed in CoTb. Based on a two-sublattice mean-field approximation, the increased compensation temperature is ascribed to the $WS_2$-mediated tuning of the magnetic moments of the sublattices Tb and Co, rather than from the changed exchange interactions $J_{\text{Co-Co}}$ and $J_{\text{Co-Tb}}$. First-principles calculations reveal that the tuned magnetic moments of the sublattices Tb and Co are realized through the proximity effect, where the charge transfer occurs between the interface of CoTb and $WS_2$. Our study proposes a viable approach to manipulate the interfacial ferrimagnetic order through the proximity effect, which has potential applications for spintronic devices.

DOI: 10.1103/PhysRevB.111.054426

## I. INTRODUCTION

Compensated rare-earth transition-metal (RE-TM) ferrimagnetic alloys have garnered considerable attention in spintronics due to their unique physical properties such as long spin coherence length, fast domain wall motion, and large spin-orbit torque [1–3]. Ferrimagnets feature as two sublattices with the opposite magnetic moments, which can be finely tuned below and above the compensation point. This is crucial to realize the net magnetization reversal, providing a novel avenue for spin-based data storage, and manipulation [4,5]. In addition, the compensated ferrimagnets exhibit a long spin coherence length, attributed to the nearly zero net effective exchange interaction averaged over the two sublattices [6]. For instance, spin currents can transport exceeding 10 nm in ferrimagnetic $[Co/Tb]_n$ multilayers [7]. Due to the negative exchange interaction between sublattices, the enhanced spin-orbit torque (SOT) are reported in these ferrimagnets [8–11]. In compensated Pt/CoGd multilayers, a remarkable nine times of the SOT effective field is observed [8]. This is also verified in Ta/CoTb bilayers, where the dampinglike SOT effective field diverges as the temperature approaches the magnetic moment compensation point [9]. More notably, the compensated ferrimagnets have faster domain wall motion driven by the current-induced SOT [12]. All the above findings indicate the importance of realizing and precisely manipulating the compensated ferrimagnetic order in spintronics.

Understanding the physics of ferrimagnetism is crucial for applications of ferrimagnetic devices. Since ferrimagnetic order depends on both the magnitude of the magnetic moments in each sublattice and their exchange interactions, controlling these parameters is essential for effective manipulation. Currently, varying exchange interactions is a widely adopted method to control ferrimagnetic order [13–16]. For example, inserting hydrogen or oxygen atoms to tune the exchange interactions between sublattices has resulted in a 130 K variation in the ferrimagnetic compensation temperature [13,14]. Similarly, strain-induced changes in the distance between magnetic atoms have altered the ferrimagnetic compensation temperature in rare-earth iron garnet (REIG) crystals by 50 K [17,18]. However, tuning the magnetic moments of ferrimagnets to manipulate ferrimagnetic order remains challenging.

Two-dimensional (2D) van der Waals materials address the challenges facing bulk magnet systems by offering new physical mechanism such as the giant spin splitting result from missing inversion symmetry [19], chiral spin textures induced by topological flat band [20], scalability, maintaining device integrity, and allowing efficient control of magnetism. The integration of van der Waals materials and ferrimagnets into heterostructures could not only introduce novel electronic phases, such as flip of the magnetic order [21], and anomalous spin current [22,23], but also tune the interfacial anisotropy [24] and magnetocrystalline anisotropy [25]. This would provide fundamental knowledge and valuable guidance for designing magnetic van der Waals heterostructures for future spintronic and valleytronic devices. As a good example of 2D van der Waals materials, $WS_2$ possesses many advantages, such as large spin-orbit coupling (spin splitting up to 426 meV) result from its broken inversion symmetry [19], and enhancing the dampinglike SOT efficiency (up to 30% with monolayer insertion) in the ferromagnet/heavy-metal

*Contact author: xueds@lzu.edu.cn

†Contact author: yangdzh@lzu.edu.cn

 

bilayer [26], making it a viable platform for the development of two-dimensional spintronic devices capable of operating. Moreover, $WS_2$ is easily prepared on a large scale promoting the development of advanced flexible devices [27]. The development of $WS_2$ based spintronic devices exhibits strong spin-dependent interactions and effective spin transport, such as the all-optical polariton spin switching [28], optotwistronic Hall effect [29], and surface charge-ordered states [30]. Thus, leveraging the proximity effect of 2D-TMDs to adjust the magnetic moments in each sublattice of ferrimagnets presents a promising approach for controlling ferrimagnetic order.

In this work, we successfully manipulated the interfacial ferrimagnetic order in $WS_2/Co_{74}Tb_{26}$ bilayers by leveraging the proximity effect of the 2D-TMDs $WS_2$. Our experimental results reveal a significant enhancement in the ferrimagnetic compensation temperature of $Co_{74}Tb_{26}$ as the count of $WS_2$ layers increases. A theoretical model based on a two-sublattice mean-field approximation shows that this substantial rise in compensation temperature is primarily due to changes in the Tb and Co magnetic moment, rather than alterations in the exchange interactions, such as $J_{\text{Co-Co}}$ and $J_{\text{Co-Tb}}$. Additionally, first-principles calculations of charge density differences confirm the enhanced charge transfer between $WS_2$ and CoTb with increasing $WS_2$ layers, aligning well with our experimental observations. These findings offer a promising approach for controlling interfacial ferrimagnetic order through the proximity effect of 2D TMDs.

## II. EXPERIMENTAL DETAILS

High-quality $WS_2$ layers of varying thicknesses were grown on a $Si/SiO_2$ substrate using chemical vapor deposition (CVD) [26]. Subsequently, a $Co_{74}Tb_{26}$ (3 nm)/Cr (3 nm)/Ti (2 nm) film was sputtered onto the surface of $WS_2$, with the Cr and Ti capping layers employed to prevent oxidation of the $Co_{74}Tb_{26}$. The $Co_{74}Tb_{26}$ alloy was fabricated by cosputtering, and its composition was precisely tuned by controlling the relative deposition rates of Co and Tb. The magnetron sputtering was conducted at a pressure below $5.0 \times 10^{-5}$ Pa at room temperature. To measure the anomalous Hall effect (AHE), the films were patterned into Hall bars with channel dimensions of 100 μm in length and 10 μm in width, as shown in Fig. 1(a). We fabricated the Hall bar according to the WS2 position, where the one Hall bar is just to cover $WS_2$, using the standard lithography and Ar ion etching. The Hall bar devices of magnetotransport configuration are wire bonded to the sample holder of CoTb/Cr/Ti. The uniformity of the device was confirmed by the energy dispersive spectrometer (EDS) tests using the scanning electron microscope (SEM). Figures 1(c) and 1(d) show the EDS measurement for Hall bars without (area 1) and with (area 2) $WS_2$ inserted, respectively. The atomic ratio (Co:Tb) exhibits 74.06:25.94, and 73.92:26.08 in the area of 1, and 2, respectively, which are both consistent with the atomic proportions of $Co_{74}Tb_{26}$ experimental estimations. Transport measurements were performed using a physical property measurement system (Quantum Design Inc., San Diego, CA) with a current of 100 μA applied. First-principles calculations were performed using the Vienna *Ab initio* Simulation Package (VASP) [31,32], which resolved the Kohn-Sham equations and employed projector augmented

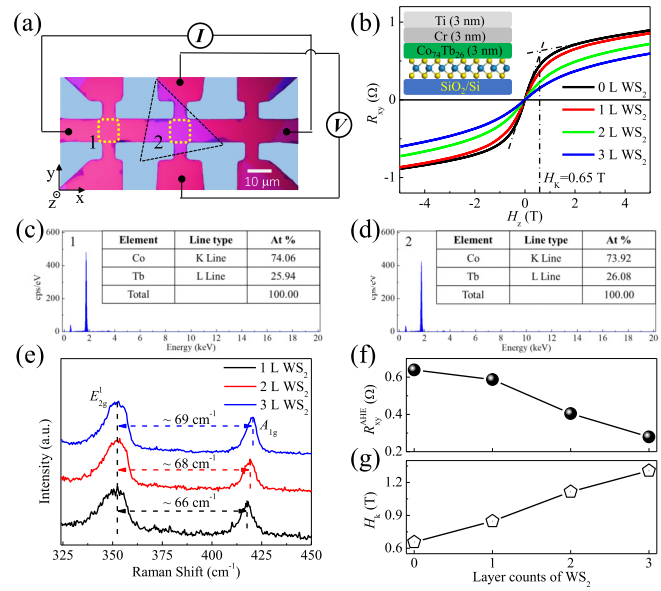


FIG. 1. (a) Schematic of the Hall bar device used for AHE electrical measurements, where the dashed triangle line represents the $WS_2$ by CVD. (b) The Hall resistance of the $WS_2$ (0–3 L)/$Co_{74}Tb_{26}$ devices by sweeping the out-of-plane field. The inset shows the view of the $WS_2/Co_{74}Tb_{26}/Cr/Ti$. The EDS measurement of (c) area 1 and (d) area 2 in (a). (e) Raman spectrum for the different $WS_2$ layer counts. The extracted (f) $R_{xy}^{AHE}$ and (g) $H_K$ with the different $WS_2$ layer counts from (b).

wave (PAW) pseudopotentials. The exchange-correlation potential was treated with the Perdew-Burke-Ernzerhof (PBE) form within the generalized gradient approximation (GGA). For structural optimization, the energy convergence threshold was set to $10^{-5}$ eV, and the residual force on each atom was reduced to less than 0.1 eV/Å. The plane-wave basis set had a cutoff energy of 400 eV, and the Brillouin zone was sampled using Γ-centered Monkhorst-Pack grids of $3 \times 3 \times 1$. The PBE functional with van der Waals (vdW) correction (vdW-DF2) was applied [33]. We adopted the DFT+U method to include effect of strongly correlated electrons [34]. The U value was set as 6 eV and 4 eV for Tb-4$f$ and Co-3$d$, respectively.

## III. RESULTS AND DISCUSSION

### A. Anomalous Hall effect

Figure 1(e) shows the typical Raman spectrum of $WS_2$, featuring the in-plane vibrational $E_{2g}^1$ mode and the out-of-plane vibrational $A_{1g}$ mode. The $E_{2g}^1$ mode exhibits minimal dependence on the layer count as the thickness of $WS_2$ increases, while a blue shift is observed in the $A_{1g}$ mode, attributed to the lattice stiffening effect from the addition of extra layers [35]. The thickness of $WS_2$ can be determined by examining the frequency difference ($\Delta\omega$) between the $A_{1g}$ and $E_{2g}^1$ modes. The $\Delta\omega$ values of approximately 66, 68, and 69 $cm^{-1}$ shown in Fig. 1(e) correspond to $WS_2$ layer counts of 1, 2, and 3 layers, respectively, consistent with previous studies [26,35].

Figure 1(b) illustrates the Hall resistance ($R_{xy}$) of $WS_2$ (0–3 L)/$Co_{74}Tb_{26}$ as a function of the out-of-plane magnetic

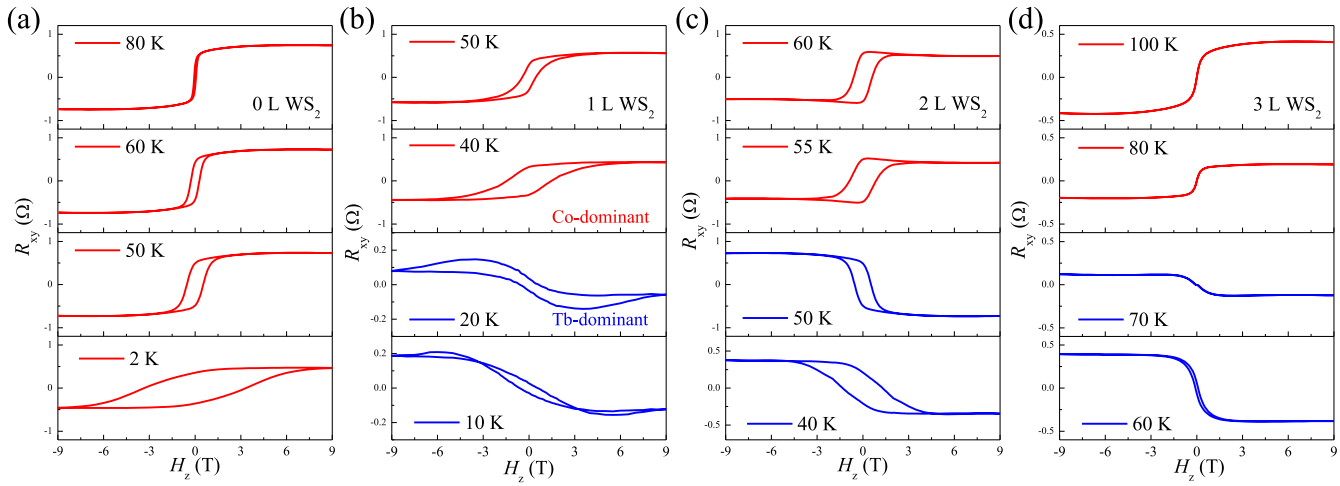


FIG. 2. AHE electrical measurement under external out-of-plane magnetic field with various temperatures for (a) 0 L, (b) 1 L, (c) 2 L, and (d) 3 L $WS_2$ inserting under $Co_{74}Tb_{26}$ film.

field ($H_z$) at room temperature. The observed Hall hysteresis loops of $Co_{74}Tb_{26}$ are similar to those of a ferromagnetic Co film [26], indicating that the magnetic moments of Co dominate in the $Co_{74}Tb_{26}$ film [9,36–39]. The tilt hysteresis loop, which exhibits almost zero coercivity, suggests that the $Co_{74}Tb_{26}$ film has in-plane magnetic anisotropy. The pronounced sharp increase in $R_{xy}$ with in-plane gradual realignment under $H_z$ is attributed to the AHE. At magnetic fields above the saturation field $H_z \approx 1.00$ T, the slow increase in $R_{xy}$ is due to the ordinary Hall effect (OHE). The out-of-plane anisotropy field ($H_K$) was obtained from the intersection point of the linear fits for the OHE and AHE, as shown in Fig. 1(b). This intersection point, representing $H_K$, indicates the magnetic moment overcomes the in-plane anisotropy energy (including demagnetization energy and surface anisotropy energy), and becomes saturated under out-of-plane magnetic field [40,41]. By subtracting the OHE contribution, we can determine the AHE resistance ($R_{xy}^{AHE}$) and $H_K$, which are strongly dependent on the count of $WS_2$ layers, as shown in Figs. 1(f) and 1(g), respectively. As the $WS_2$ layer count increases from 0–3 L, $R_{xy}^{AHE}$ decreases monotonically from 0.60–0.20 Ω, while $H_K$ increases from 0.60–1.20 T. Considering the coherent rotation model where $R_{xy}^{AHE} \propto M_S$ and $H_K \propto 1/M_S$ [42], these observations suggest that $M_S$ of $Co_{74}Tb_{26}$ can indeed be manipulated by $WS_2$ and increases with additional $WS_2$ layers, providing evidence for the proximity effect of $WS_2$ [26,43–45].

To further investigate whether the ferrimagnetic compensation temperature ($T_{comp}$) of $Co_{74}Tb_{26}$ is influenced by the proximity effect of $WS_2$, we examined the hysteresis loops of $R_{xy}$ over a broad temperature range from 2–300 K. Figure 2 displays the typical $R_{xy}$ loops near $T_{comp}$ for different $WS_2$ layer counts. At 80 K, the hysteresis loops of $Co_{74}Tb_{26}$ transition from a tilted shape to a square shape, indicating that the easy axis of the $Co_{74}Tb_{26}$ film shifts from in-plane to out-of-plane. As the temperature further decreases, the perpendicular switching field increases significantly from 0.05 T at 80 K to 3.32 T at 2 K, while the saturated value of $R_{xy}^{AHE}$ decreases gradually from 0.75–0.50 Ω. These opposing temperature-dependent behaviors can be attributed to the decrease in $M_S$ as the temperature approaches $T_{comp}$. This observation suggests that the $M_S$ of CoTb might gradually reach zero, and the $T_{comp}$ of $Co_{74}Tb_{26}$ without $WS_2$ might be below 2 K and even no compensation point.

However, upon inserting 1 L of $WS_2$ under $Co_{74}Tb_{26}$, as shown in Fig. 2(b), we observe a reversal in the polarity of the $R_{xy}^{AHE}$ loop below 40 K. This reversal implies that the magnetic moment of $WS_2$ (1 L)/$Co_{74}Tb_{26}$ becomes Tb dominated, but the spin-dependent scattering, indicated by the value of $R_{xy}^{AHE}$, remains influenced by the Co magnetic moment. This occurs because the 3*d* electrons associated with Co moments are more likely to scatter with itinerant electrons compared to the 4*f* electrons of Tb moments, which are farther from the Fermi level [46]. This result also indicates that the $T_{comp}$ of $WS_2$ (1 L)/$Co_{74}Tb_{26}$ falls between 20 and 40 K. With further increases in $WS_2$ layer counts, as shown in Figs. 2(c) and 2(d), a significant rise in $T_{comp}$ is observed. With just 3 L $WS_2$, $T_{comp}$ reaches up to 70 K.

To further elucidate the influence of different $WS_2$ layer counts on $T_{comp}$, we extracted $R_{xy}^{AHE}$ and $H_K$ as functions of temperature for $WS_2$ layer counts ranging from 0–3 L, as shown in Figs. 3(a) and 3(b), respectively. Consistent with previous reports on compensated ferrimagnet order, $H_K$ diverges as $R_{xy}^{AHE}$ approaches zero [13,18]. For the $WS_2$ layer counts of 1, 2, and 3 L, $T_{comp}$ is determined to be approximately 23 K, 61 K, and 75 K, respectively. Since the insertion of a few $WS_2$ layers does not significantly alter the strain [17,18,47] or roughness [11], the substantial enhancement in $T_{comp}$ with the addition of $WS_2$ layers strongly indicates that the manipulation of ferrimagnetic order arises from the proximity effect between $WS_2$ and CoTb.

### B. Mean-field approximation theory

To reveal and understand the fundamental mechanism behind the $WS_2$ proximity-induced changes in $T_{comp}$, we employ a two-sublattice mean-field approximation (MFA) theory to analyze the temperature dependence of magnetization in $WS_2$

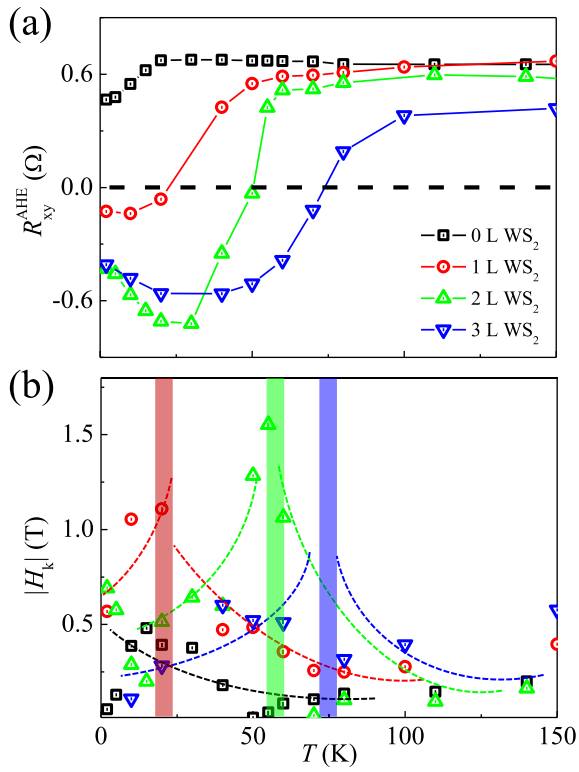


FIG. 3. The extracted (a) $R_{xy}^{AHE}$ and (b) $H_K$ as a function of temperature with the 0–3 L $WS_2$. The dashed lines are for guidance only.

(0–3 L)/$Co_{74}Tb_{26}$ bilayers [5,13,48]. The effective energy of molecular field for the two lattices is given by

$$\mu_{Co}H_{Co}^{MFA} = \mu_{Co}H + (1-p)zJ_{Co\text{-}Co}\sigma_{Co} + pzJ_{Co\text{-}Tb}\sigma_{Tb}, \quad (1a)$$

$$\mu_{Tb}H_{Tb}^{MFA} = \mu_{Tb}H + pzJ_{Tb-Tb}\sigma_{Tb} + (1-p)zJ_{Co\text{-}Tb}\sigma_{Co}, \quad (1b)$$

where $\mu_{Co}$ and $\mu_{Tb}$ are the magnetic moments of the Co and Tb sublattices, set at 1.72 and 5.39 $\mu_B$, respectively [5]. $H_{Co}^{MFA}$ and $H_{Tb}^{MFA}$ represent the molecular fields acting on the Co and Tb sublattice spins, respectively. In this model, the effective energy originates from two primary components: the Zeeman energy due to the external magnetic field $H$ and the direct exchange coupling energy. For Co spin polarization $\sigma_{Co}$, the exchange coupling energy comprises two terms: $(1-p)zJ_{Co\text{-}Co}\sigma_{Co}$, which accounts for the exchange coupling between Co atoms, with the coordination count $z = 12$, the concentration of Tb $p = 0.26$, and the exchange coupling strength $J_{Co\text{-}Co} = 18.5$ meV; and $pzJ_{Co\text{-}Tb}\sigma_{Tb}$, representing the exchange coupling between Co and Tb atoms, with $J_{Co\text{-}Tb} = -3.35$ meV. For Tb spin polarization $\sigma_{Tb}$, the exchange coupling energy is similarly considered, but the exchange coefficient $J_{Tb-Tb}$ is neglected due to its minimal impact.

To analyze the temperature dependence of sublattice magnetization, we solve the self-consistent equations for $m_{Co} = \mu_{Co}\sigma_{Co}$ and $m_{Tb} = \mu_{Tb}\sigma_{Tb}$ using standard thermodynamic statistical physics methods. The self-consistent equations are given by:

$$\sigma_{Co} = L(\xi_{Co}), \quad (2a)$$

$$\sigma_{Tb} = L(\xi_{Tb}), \quad (2b)$$

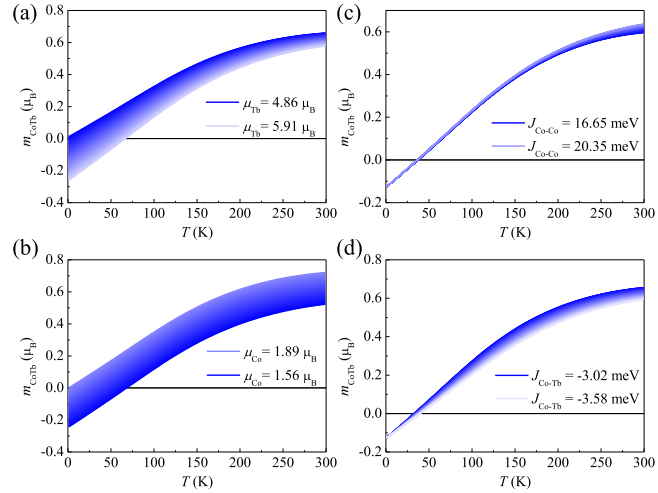


FIG. 4. The calculated $Co_{74}Tb_{26}$ magnetization as a function of temperature, by separately varying (a) $\mu_{Tb}$, (b) $\mu_{Co}$, (c) $J_{Co\text{-}Co}$, and (d) $J_{Co\text{-}Tb}$ by ±10%.

where $L(\xi) = \coth(\xi) - 1/\xi$ is the Langevin function. $\xi_i = \mu_i H_i^{MFA}/k_B T$, where $\mu_i$ is the magnetic moment of Co or Tb, $k_B$ is the Boltzmann constant and $T$ is the temperature. Therefore, the total magnetization of $Co_{74}Tb_{26}$ is given by:

$$m_{CoTb} = pm_{Tb} + (1-p)m_{Co}. \quad (3)$$

According to the MFA theory, the temperature dependence of the total magnetization of $Co_{74}Tb_{26}$ is governed by four key parameters: $\mu_{Tb}$, $\mu_{Co}$, $J_{Co\text{-}Co}$, and $J_{Co\text{-}Tb}$. To evaluate their contributions to $T_{comp}$, we calculated the temperature-dependent magnetization of the $Co_{74}Tb_{26}$ alloy, varying each parameter by ±10%. As shown in Fig. 4, the variation of $T_{comp}$ differs depending on the parameter that is varied, with the intensity of the color indicating the magnitude of the variation. The variation of $T_{comp}$ is significant and opposite when varying $\mu_{Tb}$ [Fig. 4(a)] and $\mu_{Co}$ [Fig. 4(b)], whereas it is relatively small when varying $J_{Co\text{-}Co}$ [Fig. 4(c)] and $J_{Co-Tb}$ [Fig. 4(d)]. According to our results, the observation that $T_{comp}$ of $Co_{74}Tb_{26}$ varies by approximately 75 K with the insertion of 3 L $WS_2$ suggests that the increasing $\mu_{Tb}$ and decreasing $\mu_{Co}$ could play a crucial role. At $T = 300$ K, such variations in $\mu_{Tb}$ and $\mu_{Co}$ also lead to a decrease in $m_{CoTb}$, which is consistent with the results presented in Fig. 1(f).

### C. First-principles calculations

To further demonstrate the variations of $m_{Tb}$ and $m_{Co}$ related with the proximity effect of $WS_2$, we calculated the charge density difference and magnetic moment variation of the $WS_2$ (1–3 L)/CoTb heterostructure. The results of charge density difference are presented in Figs. 5(a)–5(c), corresponding to 1–3 L $WS_2$ proximity. To eliminate interaction between periodically adjacent $WS_2$ layers, we use the thickness of the vacuum exceed 15 Å along the $z$ direction. To construct the $WS_2$/CoTb heterostructure, we take 3 × 3 $WS_2$ (1–3 L) to match 4 × 4 single layer CoTb with a minimum mismatch of lattice constants. The charge density difference ($\Delta\rho$) is obtained by subtracting the charges of $WS_2$ and CoTb from those of the heterostructure

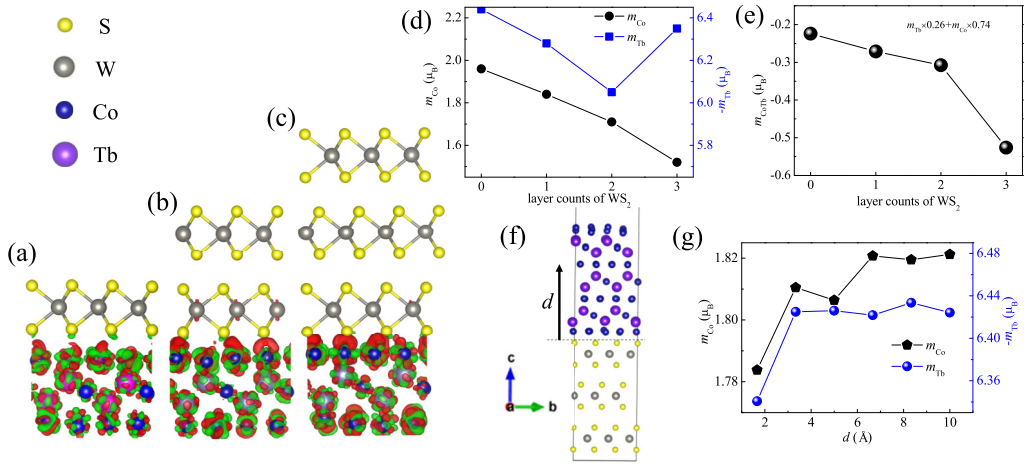


FIG. 5. The side view of the charge density differences for (a) 1 L $WS_2$/CoTb, (b) 2 L $WS_2$/CoTb, and (c) 3 L $WS_2$/CoTb, respectively. The dependence of (d) $m_{Co}$, $m_{Tb}$, and (e) $m_{CoTb}$ as a function of $WS_2$ layer counts. (f) The schematic view of heterostructures 3 L $WS_2$/CoTb. (g) The dependence of $m_{Co}$ and $m_{Tb}$ as a function of the distance between $WS_2$ interface layer.

$WS_2$/CoTb as $\Delta\rho = \rho_{(WS_2/CoTb)} - \rho_{(WS_2)} - \rho_{(CoTb)}$, where $\rho_{(WS_2/CoTb)}$, $\rho_{(WS_2)}$, and $\rho_{(CoTb)}$ are the charge densities of the heterostructure $WS_2$/CoTb, $WS_2$ and CoTb, respectively. Figures 5(a)–5(c) show side views of the calculated charge transfer at the $WS_2$ (1–3 L)/CoTb interface. The red region represents charge dissipation, and the green region indicates charge accumulation. As expected, charge transfer occurs at the $WS_2$/CoTb interface, with redistribution predominantly localized in the interface region. Notably, electron accumulation and depletion are observed around atoms at the interface, with the charge density increasing as the layer counts of $WS_2$ increases. Overall, electrons are transferred from the $WS_2$ layer to the CoTb layer, leading to a decrease in the magnetic moment of Co, while the magnetic moment of Tb initially decreases and then increases, as shown in Fig. 5(d).

Figure 5(e) shows the dependence of magnetic moment of $Co_{74}Tb_{26}$ as the layer counts of $WS_2$, which exhibit a clear enhancement as the layer counts of $WS_2$ increasing, consistent with the results presented in Fig. 1(f). This charge transfer, which reduces the magnetic moment on CoTb and leads to an increase in $T_{comp}$ of CoTb, aligns well with our experimental results. According to the first-principles calculations, we can notice that the proximity effect mainly occurs at the $WS_2$/CoTb interface, thus when CoTb is thicker, the proximity effect should be weaker [49]. Figure 5(f) further shows the magnetic moments of Co and Tb at different distance $d$ from the $WS_2$/CoTb interface. As we expected, the magnetic moment of Co is sharply decreased ∼20% and Tb atoms is slightly decrease ∼10% due to interface proximity effect. But when $d$ is far beyond 4 Å, the magnetic moments of Co and Tb atoms gradually stabilize, also confirming its interface effect, as shown in Fig. 5(g). Then, we will explain why we could still experimentally observe a significant change in compensation temperature even if the thickness of CoTb is reach up 3 nm. This is because we utilized the spin transport measurement to investigate the compensation temperature of CoTb. As we known, when charge current is applied, electrons with opposite spin directions will transversely move towards the opposite directions and accumulate at the edges. If the opposite spin numbers are not equal (also called spin-polarized current), then a net charge accumulation is formed and manifested itself as a Hall voltage. Such spin-polarized current is not only filtered by bulk magnetization of CoTb, but also is caused by the interface scattering due to the interface net magnetization. Considering a very long spin diffusion length (10 nm) in compensated ferrimagnets CoTb [7], the spin-polarized current induced by interface scattering should be dominant, which can also form a significant AHE voltage when CoTb is 3 nm.

## IV. CONCLUSION

In summary, we demonstrate a method to effectively control the interfacial ferrimagnetic order and $T_{comp}$ of CoTb through the proximity effect of $WS_2$. By inserting varying layers of 2D $WS_2$, we achieve a notable enhancement in $T_{comp}$, with an increase of up to 75 K observed for 3 L $WS_2$. The temperature dependence of the magnetization, modeled using MFA simulations, corroborates the observed enhancement in $T_{comp}$ with increasing $WS_2$ layers. First-principles calculations further support these results by revealing the modulation of magnetic moments in the CoTb alloy as a function of $WS_2$ layer count. These findings present a viable pathway for tailoring material properties in ferrimagnetic-based spintronic devices.

## ACKNOWLEDGMENTS

This work is supported by the National Key R&D Program of China (No. 2021YFB3501300), NSFC of China (Grants No. 12474116, and No. 12174163), the Postdoctoral Fellowship Program of CPSF (Grant No. GZC20230997), Natural Science Foundation of Gansu Province (Grant No. 24JRRA523), and China Postdoctoral Science Foundation (Grant No. 2024T170368).

[1] S. K. Kim, G. S. D. Beach, K.-J. Lee, T. Ono, T. Rasing, and H. Yang, Ferrimagnetic spintronics, Nat. Mater. **21**, 24 (2022).

[2] G. Sala and P. Gambardella, Ferrimagnetic dynamics induced by spin-orbit torques, Adv. Mater. Interfaces **9**, 2201622 (2022).

[3] Y. Zhang, X. Feng, Z. Zheng, Z. Zhang, K. Lin, X. Sun, G. Wang, J. Wang, J. Wei, P. Vallobra, Y. He, Z. Wang, L. Chen, K. Zhang, Y. Xu, and W. Zhao, Ferrimagnets for spintronic devices: From materials to applications, Appl. Phys. Rev. **10**, 011301 (2023).

[4] J.-H. Park, W. T. Kim, W. Won, J.-H. Kang, S. Lee, B.-G. Park, B. S. Ham, Y. Jo, F. Rotermund, and K.-J. Kim, Observation of spin-glass-like characteristics in ferrimagnetic TbCo through energy-level-selective approach, Nat. Commun. **13**, 5530 (2022).

[5] D. H. Suzuki, M. Valvidares, P. Gargiani, M. Huang, A. E. Kossak, and G. S. D. Beach, Thickness and composition effects on atomic moments and magnetic compensation point in rare-earth transition-metal thin films, Phys. Rev. B **107**, 134430 (2023).

[6] P. M. Haney and A. H. MacDonald, Current-induced torques due to compensated antiferromagnets, Phys. Rev. Lett. **100**, 196801 (2008).

[7] J. Yu, D. Bang, R. Mishra, R. Ramaswamy, J. H. Oh, H.-J. Park, Y. Jeong, P. Van Thach, D.-K. Lee, G. Go, S.-W. Lee, Y. Wang, S. Shi, X. Qiu, H. Awano, K.-J. Lee, and H. Yang, Long spin coherence length and bulk-like spin–orbit torque in ferrimagnetic multilayers, Nat. Mater. **18**, 29 (2019).

[8] R. Mishra, J. Yu, X. Qiu, M. Motapothula, T. Venkatesan, and H. Yang, Anomalous current-induced spin torques in ferrimagnets near compensation, Phys. Rev. Lett. **118**, 167201 (2017).

[9] K. Ueda, M. Mann, P. W. P. de Brouwer, D. Bono, and G. S. D. Beach, Temperature dependence of spin-orbit torques across the magnetic compensation point in a ferrimagnetic TbCo alloy film, Phys. Rev. B **96**, 064410 (2017).

[10] Z. Zheng, Y. Zhang, X. Feng, K. Zhang, J. Nan, Z. Zhang, G. Wang, J. Wang, N. Lei, D. Liu, Y. Zhang, and W. Zhao, Enhanced spin-orbit torque and multilevel current-induced switching in W/Co-Tb/Pt heterostructure, Phys. Rev. Appl. **12**, 044032 (2019).

[11] H. Xue, W. Lv, D. Wu, J. Cai, Z. Ji, Y. Zhang, Z. Zeng, Q. Jin, and Z. Zhang, Temperature dependence of spin–orbit torques in nearly compensated $Tb_{21}Co_{79}$ films by a topological insulator $Sb_2Te_3$, J. Phys. Chem. Lett. **12**, 2394 (2021).

[12] Y. Zhou, T. Xu, X. Liang, L. Zhao, H.-A. Zhou, Z. Wang, W. Jiang, and Y. Zhou, A comparative study of the domain wall motion in ferrimagnets $(Fe,Co)_{1-x}(Gd,Tb)_x$, Nanoscale **14**, 13526 (2022).

[13] M. Huang, M. U. Hasan, K. Klyukin, D. Zhang, D. Lyu, P. Gargiani, M. Valvidares, S. Sheffels, A. Churikova, F. Büttner, J. Zehner, L. Caretta, K.-Y. Lee, J. Chang, J.-P. Wang, K. Leistner, B. Yildiz, and G. S. D. Beach, Voltage control of ferrimagnetic order and voltage-assisted writing of ferrimagnetic spin textures, Nat. Nanotechnol. **16**, 981 (2021).

[14] X. Feng, Z. Zheng, Y. Zhang, Z. Zhang, Y. Shao, Y. He, X. Sun, L. Chen, K. Zhang, P. Khalili Amiri, and W. Zhao, Magneto-ionic control of ferrimagnetic order by oxygen gating, Nano Lett. **23**, 4778 (2023).

[15] A. V. Svalov, V. O. Vas'kovskiy, V. N. Lepalovskij, A. Larrañaga, and G. V. Kurlyandskaya, Structure and magnetic properties of Tb-Co/Ti and Tb-Co/$Al_2O_3$ multilayers, J. Magn. Magn. Mater. **465**, 147 (2018).

[16] M. Martini, C. O. Avci, S. Tacchi, C.-H. Lambert, and P. Gambardella, Engineering the spin-orbit-torque efficiency and magnetic properties of Tb/Co ferrimagnetic multilayers by stacking order, Phys. Rev. Appl. **17**, 044056 (2022).

[17] T. Bayaraa, C. Xu, D. Campbell, and L. Bellaiche, Tuning magnetization compensation and Curie temperatures in epitaxial rare earth iron garnet films, Phys. Rev. B **100**, 214412 (2019).

[18] Y. Li, X. Yang, H. Bai, M. Wang, D. Cheng, C. Song, Z. Yuan, Y. Liu, and Z. Shi, Strain-tunable magnetic compensation temperature of epitaxial $Tb_3Fe_5O_{12}$ thin films, Phys. Rev. B **108**, 184403 (2023).

[19] Z. Y. Zhu, Y. C. Cheng, and U. Schwingenschlögl, Giant spin-orbit-induced spin splitting in two-dimensional transition-metal dichalcogenide semiconductors, Phys. Rev. B **84**, 153402 (2011).

[20] N. Paul, Y. Zhang, and L. Fu, Giant proximity exchange and flat Chern band in 2D magnet-semiconductor heterostructures, Sci. Adv. **9**, eabn1401 (2023).

[21] K. L. Seyler, D. Zhong, B. Huang, X. Linpeng, N. P. Wilson, T. Taniguchi, K. Watanabe, W. Yao, D. Xiao, M. A. McGuire, K.-M. C. Fu, and X. Xu, Valley manipulation by optically tuning the magnetic proximity effect in $WSe_2/CrI_3$ heterostructures, Nano Lett. **18**, 3823 (2018).

[22] F. Wang, G. Shi, K.-W. Kim, H.-J. Park, J. G. Jang, H. R. Tan, M. Lin, Y. Liu, T. Kim, D. Yang, S. Zhao, K. Lee, S. Yang, A. Soumyanarayanan, K.-J. Lee, and H. Yang, Field-free switching of perpendicular magnetization by two-dimensional $PtTe_2/WTe_2$ van der Waals heterostructures with high spin Hall conductivity, Nat. Mater. **23**, 768 (2024).

[23] Y. Dai, J. Xiong, Y. Ge, B. Cheng, L. Wang, P. Wang, Z. Liu, S. Yan, C. Zhang, X. Xu, Y. Shi, S.-W. Cheong, C. Xiao, S. A. Yang, S.-J. Liang, and F. Miao, Interfacial magnetic spin Hall effect in van der Waals $Fe_3GeTe_2/MoTe_2$ heterostructure, Nat. Commun. **15**, 1129 (2024).

[24] G. Wu, D. Wang, N. Verma, R. Rao, Y. Cheng, S. Guo, G. Cao, K. Watanabe, T. Taniguchi, C. N. Lau, F. Yang, M. Randeria, M. Bockrath, and P. C. Hammel, Enhancing perpendicular magnetic anisotropy in garnet ferrimagnet by interfacing with few-layer $WTe_2$, Nano Lett. **22**, 1115 (2022).

[25] Z. Tu, T. Zhou, T. Ersevim, H. S. Arachchige, A. T. Hanbicki, A. L. Friedman, D. Mandrus, and M. Ouyang, Spin–orbit coupling proximity effect in $MoS_2/Fe_3GeTe_2$ heterostructures, Appl. Phys. Lett. **120**, 043102 (2022).

[26] Y. Li, Y. Song, J. Zhang, Q. Yang, L. Xi, Y. Zuo, J. Zhang, M. Si, D. Xue, and D. Yang, Enhancement of spin-orbit torque in $WS_2$/Co/Pt trilayers via spin-orbit proximity effect, Phys. Rev. B **107**, L100403 (2023).

[27] X. Song, R. Singha, G. Cheng, Y.-W. Yeh, F. Kamm, J. F. Khoury, B. L. Hoff, J. W. Stiles, F. Pielnhofer, P. E. Batson, N. Yao, and L. M. Schoop, Synthesis of an aqueous, air-stable, superconducting 1T'-$WS_2$ monolayer ink, Sci. Adv. **9**, eadd6167 (2023).

[28] J. Zhao, A. Fieramosca, R. Bao, K. Dini, R. Su, D. Sanvitto, Q. Xiong, and T. C. H. Liew, Room temperature polariton spin switches based on Van der Waals superlattices, Nat. Commun. **15**, 7601 (2024).

[29] Z. Ji, Y. Zhao, Y. Chen, Z. Zhu, Y. Wang, W. Liu, G. Modi, E. J. Mele, S. Jin, and R. Agarwal, Opto-twistronic Hall effect in a three-dimensional spiral lattice, Nature (London) **634**, 69 (2024).

[30] Y. Yang, Q. Tao, Y. Fang, G. Tang, C. Yao, X. Yan, C. Jiang, X. Xu, F. Huang, W. Ding, Y. Wang, Z. Mao, H. Xing, and Z.-A. Xu, Anomalous enhancement of the Nernst effect at the crossover between a Fermi liquid and a strange metal, Nat. Phys. **19**, 379 (2023).

[31] G. Kresse and J. Furthmuller, Efficiency of *ab-initio* total energy calculations for metals and semiconductors using a plane-wave basis set, Comput. Mater. Sci. **6**, 15 (1996).

[32] G. Kresse and J. Furthmuller, Efficient iterative schemes for *ab initio* total-energy calculations using a plane-wave basis set, Phys. Rev. B **54**, 11169 (1996).

[33] S. Grimme, Semiempirical GGA-type density functional constructed with a long-range dispersion correction, J. Comput. Chem. **27**, 1787 (2006).

[34] V. I. Anisimov, J. Zaanen, and O. K. Andersen, Band theory and Mott insulators: Hubbard *U* instead of Stoner *I*, Phys. Rev. B **44**, 943 (1991).

[35] H. Zeng, G.-B. Liu, J. Dai, Y. Yan, B. Zhu, R. He, L. Xie, S. Xu, X. Chen, W. Yao, and X. Cui, Optical signature of symmetry variations and spin-valley coupling in atomically thin tungsten dichalcogenides, Sci. Rep. **3**, 1608 (2013).

[36] J. Finley and L. Liu, Spin-orbit torque efficiency in compensated ferrimagnetic cobalt-terbium alloys, Phys. Rev. Appl. **6**, 054001 (2016).

[37] K. Ueda, M. Mann, C.-F. Pai, A.-J. Tan, and G. S. D. Beach, Spin-orbit torques in $Ta/Tb_xCo_{100-x}$ ferrimagnetic alloy films with bulk perpendicular magnetic anisotropy, Appl. Phys. Lett. **109**, 232403 (2016).

[38] P. Hansen, C. Clausen, G. Much, M. Rosenkranz, and K. Witter, Magnetic and magneto-optical properties of rare-earth transition-metal alloys containing Gd, Tb, Fe, Co, J. Appl. Phys. **66**, 756 (1989).

[39] S. Alebrand, M. Gottwald, M. Hehn, D. Steil, M. Cinchetti, D. Lacour, E. E. Fullerton, M. Aeschlimann, and S. Mangin, Light-induced magnetization reversal of high-anisotropy TbCo alloy films, Appl. Phys. Lett. **101**, 162408 (2012).

[40] L. Liu, O. J. Lee, T. J. Gudmundsen, D. C. Ralph, and R. A. Buhrman, Current-induced switching of perpendicularly magnetized magnetic layers using spin torque from the spin Hall effect, Phys. Rev. Lett. **109**, 096602 (2012).

[41] H. Hayashi, A. Asami, and K. Ando, Anomalous Hall effect at a $PtO_x$/Co interface, Phys. Rev. B **100**, 214415 (2019).

[42] S. Sangiao, L. Morellon, G. Simon, J. M. De Teresa, J. A. Pardo, J. Arbiol, and M. R. Ibarra, Anomalous Hall effect in Fe (001) epitaxial thin films over a wide range in conductivity, Phys. Rev. B **79**, 014431 (2009).

[43] H. Da, Magneto-optic effects of monolayer transition metal dichalcogenides induced by ferrimagnetic proximity effect, Phys. B: Condens. Matter **640**, 414073 (2022).

[44] K. Dolui, M. D. Petrović, K. Zollner, P. Plecháč, J. Fabian, and B. K. Nikolić, Proximity spin–orbit torque on a two-dimensional magnet within van der waals heterostructure: Current-driven antiferromagnet-to-ferromagnet reversible nonequilibrium phase transition in bilayer $CrI_3$, Nano Lett. **20**, 2288 (2020).

[45] K. Dolui and B. K. Nikolic, Spin-orbit-proximitized ferromagnetic metal by monolayer transition metal dichalcogenide: Atlas of spectral functions, spin textures, and spin-orbit torques in $Co/MoSe_2$, $Co/WSe_2$, and $Co/TaSe_2$ heterostructures, Phys. Rev. Mater. **4**, 104007 (2020).

[46] M. Wietstruk, A. Melnikov, C. Stamm, T. Kachel, N. Pontius, M. Sultan, C. Gahl, M. Weinelt, H. A. Durr, and U. Bovensiepen, Hot-electron-driven enhancement of spin-lattice coupling in Gd and Tb 4*f* ferromagnets observed by femtosecond X-ray magnetic circular dichroism, Phys. Rev. Lett. **106**, 127401 (2011).

[47] J. Wang, M. Li, C. Li, R. Tang, M. Si, G. Chai, J. Yao, C. Jia, and C. Jiang, Piezostrain-controlled magnetization compensation temperature in ferrimagnetic GdFeCo alloy films, Phys. Rev. B **107**, 184424 (2023).

[48] T. A. Ostler, R. F. L. Evans, R. W. Chantrell, U. Atxitia, O. Chubykalo-Fesenko, I. Radu, R. Abrudan, F. Radu, A. Tsukamoto, A. Itoh, A. Kirilyuk, T. Rasing, and A. Kimel, Crystallographically amorphous ferrimagnetic alloys: Comparing a localized atomistic spin model with experiments, Phys. Rev. B **84**, 024407 (2011).

[49] I. Žutić, A. Matos-Abiague, B. Scharf, H. Dery, and K. Belashchenko, Proximitized materials, Mater. Today **22**, 85 (2019).